Geology

Stress- and fluid-driven failure during fracture array growth: Implications for coupled deformation and fluid flow in the crust

Auke Barnhoorn, Stephen F. Cox, David J. Robinson and Tim Senden

Geology 2010;38;779-782
doi: 10.1130/G31010.1

Notes

Stress- and fluid-driven failure during fracture array growth: Implications for coupled deformation and fluid flow in the crust

Auke Barnhoorn[1,2,*], Stephen F. Cox[1], David J. Robinson[1,3], and Tim Senden[4]
[1]Research School of Earth Sciences, Australian National University, Canberra, ACT 0200, Australia
[2]Faculty of Geosciences, Utrecht University, 3508 TC Utrecht, Netherlands
[3]Risk and Impact Analysis Group, Geoscience Australia, Canberra, ACT 2601, Australia
[4]Department of Applied Mathematics, Research School of Physics and Engineering, Australian National University, Canberra, ACT 0200, Australia

ABSTRACT

Brittle experimental deformation on dolomite rocks shows for the first time the difference in growth of fracture networks by ordinary percolation and invasion percolation processes. Stress-driven fracture growth, in the absence of fluid pressure, is an ordinary percolation process characterized by distributed nucleation and growth of microfractures, which coalesce with increasing strain to form a connected fracture network. Fluid pressure–driven fracture growth is more akin to an invasion percolation process characterized by preferential fracture growth occurring initially at the high fluid pressure part of the rock. With progressive deformation, the network propagates rapidly through the sample and away from the high fluid pressure reservoir. X-ray microtomography analysis suggests that the fracture network in three dimensions (3-D) is probably a fully connected network at peak stress conditions, whereas conventional 2-D analysis suggests that connectivity only occurs at shear failure. The development of 3-D fracture connectivity prior to shear failure has important implications for fluid flow and fluid pressure changes immediately prior to rupture nucleation in active fault zones, for fluid migration in ore-producing hydrothermal systems, and for reservoir integrity in hydrocarbon systems.

INTRODUCTION

The geometry and connectivity of fracture networks have primary control on processes such as fluid flow in hydrothermal systems, formation of ore deposits, petroleum reservoir performance, and the evolution of fluid pressure and stress states during earthquake cycles (Hickman et al., 1995; Cox, 1999; Sibson, 2000, 2007; Berkowitz, 2002; Miller et al., 2004; Tripp and Vearncombe, 2004). In particular, when growth of fractures first creates a connected fracture network through a rock (i.e., the percolation threshold; Sahimi, 1994; Stark and Stark, 1991), there can be a drastic change in the mechanical and fluid transport properties of the rock. The formation of fracture networks at depth can be driven by changes in both stress states and fluid pressures (Sibson, 1996). Cox (2005, 2007) suggested that fracture networks may evolve differently, depending on whether fracture growth is driven by stress changes or fluid pressure changes. During stress-driven growth of fracture networks in isotropic rocks, fractures can form anywhere throughout the sample when stresses exceed the local yield strength of the rock. With continuing deformation, fractures grow and nucleate, increasing the fracture connectivity. This fracture network process is an example of ordinary percolation.

At a differential stress smaller than the dry yield strength (i.e., no fractures yet present), an increase in pore pressure can reduce the effective pressure sufficiently to lead to failure. Elevated pore-fluid pressures at fracture tips, in a network connected to a high fluid pressure reservoir, may result in propagation of the network further into the rock mass. This fluid pressure–driven fracture process is an example of an invasion percolation process.

Calcite marble deformation experiments studied the strength and permeability evolution during (semi-)brittle deformation due to changes in confining pressure, pore-fluid pressure, temperature, and grain size (e.g., Fischer and Paterson, 1992; Fredrich et al., 1990; Zhang et al., 1994). Here we examine the growth and morphology of microfracture networks in dolomite marble formed at elevated confining pressures during loading in the absence of pore fluid, and contrast this with fracture networks formed at approximately constant differential stress, but in a regime with high fluid pressures at one end of a sample. Fracture network characterization in two and three dimensions (2-D, 3-D) was carried out using scanning electron microscopy and X-ray microtomography techniques.

EXPERIMENTAL METHODOLOGY

The dolomitic marble contains minor amounts (<2%) of calcite and sheet silicates. It has no visible porosity and thus a very low permeability. The grain size is large (mean is ~1.4 mm, minimum is ~0.4 mm, and maximum is ~4 mm) with highly lobate grain boundaries, and some twinning.

Deformation experiments were conducted on specimens (length l ~22 mm and diameter ϕ = 10 mm) in a Paterson gas apparatus having independent control of confining pressure (P_c), pore-fluid pressure (P_p), and strain rate ($\dot{\varepsilon}$). Two types of triaxial deformation experiments were performed at room temperature: (1) brittle failure driven by increasing differential stress at nominally constant strain rate in the absence of a pore fluid, and (2) brittle failure driven by increasing fluid pressure at one end of the sample at approximately constant differential stress. First, P_c was raised to 50 MPa (experiments without a pore fluid) or 100 MPa (experiments with a pore fluid). Specimens were then shortened axially at a nominal $\dot{\varepsilon}$ of 2×10^{-6} – 1×10^{-5} s^{-1}. Experiments in the absence of fluid pressures were terminated at three different strains (Fig. 1; Table DR1 in the GSA Data Repository[1]) that illustrated the growth of the fracture network. In the elevated fluid pressure experiments, loading was stopped at stresses just below the yield strength. Subsequently P_p at the top of the specimen was raised to typically $0.5P_c$ – $0.8P_c$ and maintained at high levels for varying amounts of time (Table DR1). Deionized water was used as pore fluid. Effective confining pressures were high enough to prevent pore fluid leakage along the Cu jacket–sample interface. The experiments simulate natural, low-permeability rocks under stress that, due to the presence of a local high fluid pressure reservoir and reduced effective pressures, fail adjacent to the reservoir. Continuous supply of fluids and maintenance of high fluid pressures can cause a propagation of the fracture network away from the reservoir. Fluids were initially absent at the bottom of the specimens. Drained conditions at the bottom allowed fluids to escape and prevented buildup of significant fluid pressure in that area.

Fracture networks in longitudinal specimen sections were imaged by backscattered electron

*E-mail: auke.barnhoorn@geo.uu.nl.

[1]GSA Data Repository item 2010220, Table DR1 (experimental details and fracture characteristics), is available online at www.geosociety.org/pubs/ft2010.htm, or on request from editing@geosociety.org or Documents Secretary, GSA, P.O. Box 9140, Boulder, CO 80301, USA.

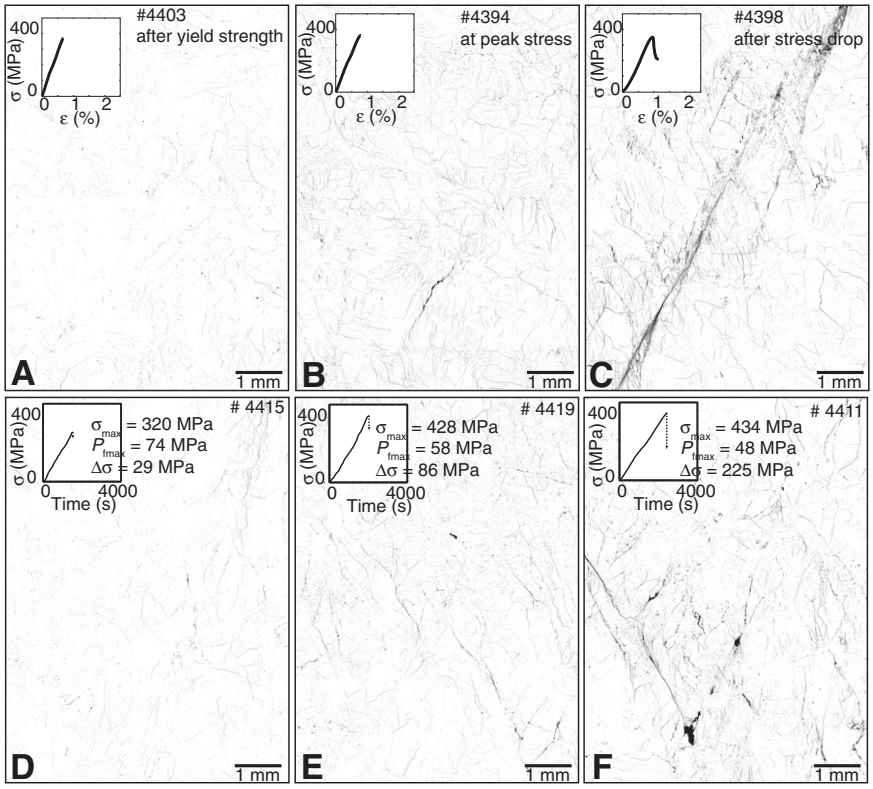

Figure 1. A–C: Two-dimensional fracture networks (samples 4403, 4394, and 4398) deformed to increasing strain (no elevated fluid pressures). Images are thresholded backscattered electron images. Black pixels represent fractures and white pixels represent unfractured dolomite grains and grain boundaries. D–F: Fracture networks (samples 4415, 4419, and 4411) in presence of elevated fluid pressures. Insets indicate σ-ε history in A–C and σ-t history in D–F and maximum values of σ_1, P_{fmax}, and stress drop (Δσ). Images show approximately top two-thirds of samples.

imaging (BSE) in a scanning electron microscope in which open fractures within and along grains are black; the fracture-free dolomite grain interiors, grain boundaries, and minor secondary phases have a gray color. Mosaics of all images were thresholded, producing images in which black pixels represent fractures and white pixels represent unfractured material. Analyses using a MATLAB object recognition and connectivity routine provided estimates of fracture densities (the fraction of the area taken up by black pixels; i.e., fractures) across the sample, fracture lengths, and fracture abundances (number of fractures present).

Part of the fracture network in sample 4394 (P_c = 50 MPa, deformed to just after yield stress) was imaged in 3-D using microcomputed X-ray tomography (Sakellariou et al., 2004). A cylinder with ϕ = 2.5 mm and l = 5 mm was cored from the central part of sample 4394 and imaged using X-rays over a 360° rotation with 0.125° intervals. The 2880 images were reconstructed using a modified Feldcamp algorithm to give a (2048)^3 voxel tomogram with a unit voxel edge length of 1.44 μm. The grayscale values in the data set correspond to apparent X-ray attenuation. A partially filled voxel will show a lower density than the surrounding parent material. This information is used during segmentation to determine if a given voxel is one material phase or another (or void). Density contrasts between dolomite and fractures (voids) were depicted by the analysis and a 3-D image of the fracture network was constructed. Connectivity analysis of the fracture network was performed to determine whether the different fractures belong to a connected 3-D fracture network.

RESULTS

Fracture Growth in the Absence of Elevated Fluid Pressures

The 2-D microstructure of the sample, deformed at P_c = 50 MPa until just after the yield strength, is characterized by the formation of a large number of small fractures distributed approximately evenly throughout the sample (Fig. 1A). The fracture density (area taken up by black pixels) is small (0.24%), but does not vary significantly from top to bottom of the sample. With increasing deformation to peak stress conditions (Fig. 1B), continued formation of fractures is indicated by an increase in number of individual fractures per square millimeter, the larger number of fractures with intermediate and larger lengths (Fig. 2A; Table DR1), and an increased fracture density (1.2%). However, the individual fractures do not form a single, large, throughgoing fracture network in 2-D. Only locally, some sets of fractures form small-scale connected, but isolated clusters. The log-log plot of fracture abundance versus fracture length for experiments 4403 and 4394 (Fig. 2A) shows a gradual decrease in slope with increasing strain, possibly indicating that an increasing proportion of fracture length is controlled by growth rather than nucleation. After peak stress (Fig. 1C), rapid weakening is associated with the formation of a shear failure zone inclined at 27°–30° to the maximum principal stress (vertical in Fig. 1). Although the fracture density and average length of the fractures have increased, the number of individual fractures per square millimeter has decreased, indicating that individual fractures have coalesced and formed a connected network of fractures during shear failure. The change in slope of fracture abundance toward larger fracture lengths for 4398 (Fig. 2A) indicates that a larger proportion of the fractures are longer than in the lower strain experiments. This suggests that fracture length is influenced by individual fractures joining up, as well as by nucleation and growth of individual fractures. Fracture density variations within the sample 4398 are somewhat larger than in the less deformed samples, but a systematic trend is absent.

Fracture Growth in the Presence of Elevated Fluid Pressures

Samples were triaxially loaded to a differential stress just below the yield strength of dolomite at room temperature and P_c = 100 MPa. Subsequent gradual increase in P_p at the top of the sample to 50–80 MPa resulted in a slight stress relaxation, indicating that the lowered effective pressure facilitated fracture nucleation and growth.

Fracture growth microstructures are based on three experiments (4419, 4415, and 4411) held at high fluid pressures for various durations of stress relaxation (Figs. 1D–1F). The fracture density increases with increasing stress relaxation at constant fluid pressure. For samples 4415 and 4419 (Figs. 1D, 1E, and 2D), although the fracture density distribution from the top to the bottom of the samples is very irregular, there is a distinct, but modest decrease in mean fracture density (linear fit) from the top to the bottom of the sample (Fig. 2D). This fracture density decrease is absent in the third, more highly strained sample (4411, Figs. 1F and 2D), which contains large networks of connected fractures, including two well-developed sets of conjugate shear failure zones. The large pores (middle and bottom of Fig. 1F) are interpreted to have been

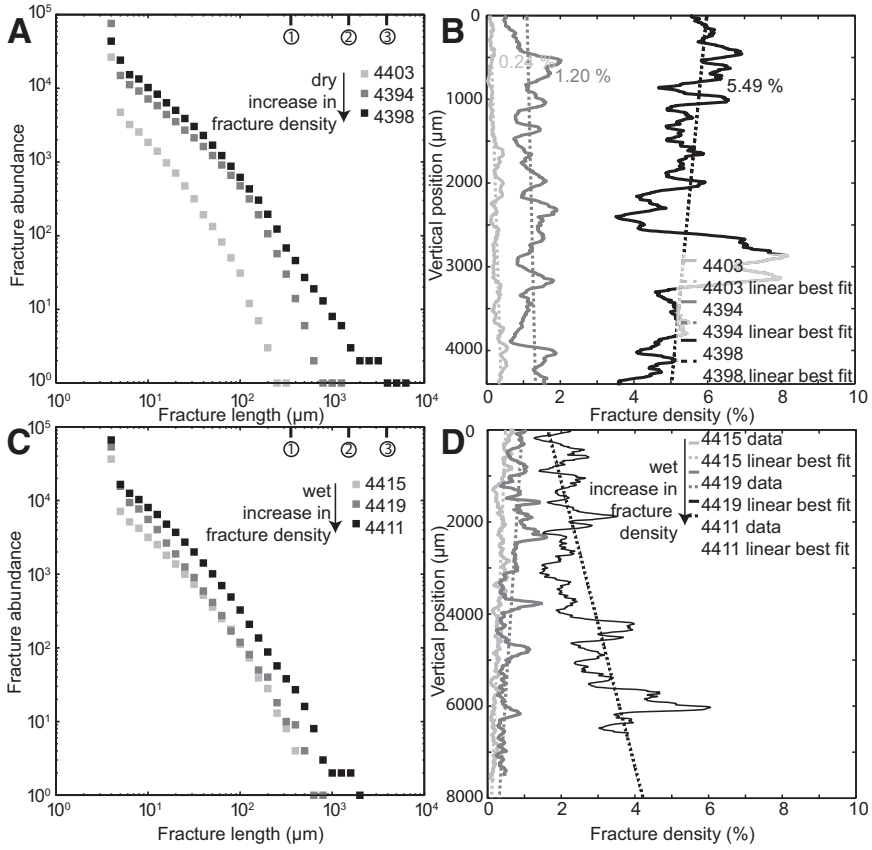

Figure 2. A, C: Fracture abundance (total number of fractures) with lengths larger than certain length versus fracture length. B, D: Fracture density trends from top to bottom of sample for (A and B) samples deformed in absence of fluid and (C and D) in presence of elevated fluid pressures. Symbols 1, 2, and 3 indicate minimum (0.35 mm), mean (1.4 mm), and maximum (4 mm) grain sizes.

caused by preferential plucking of dolomite during polishing and have been removed from the fracture density trend in Figure 2D.

It is significant that all samples deformed at elevated pore pressures contain fractures throughout the sample. The fractures with the largest lengths are present at the top of the sample in the region adjacent to the high pore pressure fluid reservoir (e.g., top right corner of Fig. 1D). The fracture length distribution in Figure 2C shows only a very small evolution in the distribution of fractures. A smaller number of larger fractures is formed than in the absence of an elevated fluid pressure (Fig. 2A) and the change in the slope of the relationship between fracture abundance and fracture length, observed at large fracture lengths in sample 4398 (Fig. 2A), is absent.

3-D Fracture Network

Sample 4394 (deformed to peak stress in the absence of fluid pressure) was analyzed using the microcomputed X-ray tomography technique (Fig. 3). The voxel size (1.44 μm) is smaller than the aperture width of the majority of the fractures. In addition, density contrast between the dolomite grains and the air-filled fractures is sufficiently large for most fractures to be resolved. The computed 3-D image therefore successfully visualizes the fractures and shows that multiple fractures with various orientations occur in the analyzed part of the sample. Connectivity analyses of the fractures in 3-D show that the individual fractures are highly interconnected. Therefore, the fractures form a connected network in 3-D prior to pervasive shear failure.

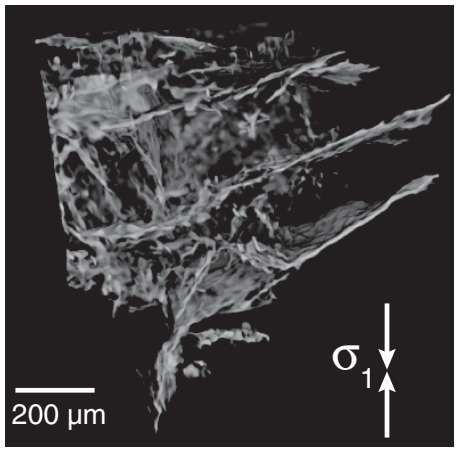

Figure 3. Three-dimensional image of fracture network produced by X-ray microtomography in small volume of sample 4394.

The volume of the cylinder analyzed by microtomography (ϕ = 2.5 mm, l = 5 mm) is much smaller than the total sample volume (ϕ = 10 mm, l ~ 22 mm). However, 2-D analysis of fractures across an area of the same size in a similar part of this sample indicates that the individual fractures are not yet fully connected in 2-D (Fig. 1B). By assuming that the observed 3-D connectivity is representative for the whole sample, it can be concluded that fracture connectivity is achieved prior to peak stress conditions.

DISCUSSION AND IMPLICATIONS

Onset of Fracture Connectivity

A key point to emerge is that high fracture densities are well developed prior to pervasive shear failure in dolomite deformed at low effective confining pressures (P_c = 50–100 MPa). The 2-D fracture connectivity analysis suggests that full connectivity (i.e., the percolation threshold) is not attained until the onset of pervasive shear failure. However, the combination of 3-D X-ray tomography and 2-D analysis indicates that a connected network of fractures, and hence the fluid percolation threshold, is developed prior to peak stress conditions. The lack of 2-D connectivity at this stage suggests that connected pathways are very tortuous in 3-D. This result explains previous work (e.g., Fischer and Paterson, 1992; Zhang et al., 1994; Peach and Spiers, 1996; De Paola et al., 2009) in which growth and connectivity of intragranular and intergranular fractures prior to pervasive shear failure was accompanied by large permeability increases. Transgranular fractures occur predominantly in the main shear failure zone and developed after peak stress conditions. The results indicate that major, fracture-controlled permeability enhancement can be achieved at very low strains in brittle and brittle-ductile regimes.

Fluid-Driven Growth of Fracture Networks

In the earliest stages of network growth in experiments with high fluid pressures at one end of the sample (Figs. 1D and 1E), mean fracture densities are highest adjacent to the upstream end of the sample that abuts the pressurized fluid reservoir; there is a weak, but significant decrease in mean fracture density toward the downstream end of the sample (Fig. 2D). This contrasts with nearly uniform mean fracture density at the early stages of network growth in experiments without fluid pressures. This observation confirms that elevated fluid pressures

can stimulate growth of fracture networks via an invasion percolation process. Purely stress-driven growth with essentially uniform mean fracture densities is more akin to an ordinary percolation process.

The fracture density trend for sample 4411 (Figs. 1F and 2D) is interpreted to indicate that, once the fluid percolation threshold is reached, further increase in fracture density occurs uniformly throughout the sample volume.

Implications for Fracture-Controlled Flow Systems

Three key outcomes have implications for understanding the dynamics of fluid migration in fracture-controlled flow regimes: (1) fluid-driven failure generates fracture networks by invasion percolation processes, (2) rapid propagation of microfractures allows fracture arrays to reach the fluid percolation threshold prior to peak stress at low effective confining pressures, and (3) change occurs from tortuous 3-D–connected, low-aperture, grain-scale pathways prior to peak stress conditions, to flow within throughgoing or short-circuit pathways, along brittle shear failure zones at shear failure.

The results have particular application for understanding the mechanical behavior of active fault systems that penetrate overpressured fluid reservoirs. During tectonic loading, overpressured parts of a fault will approach the failure condition first, whereas domains in the fault, where pore fluid factor is lower, will have stress and fluid pressure states further from the failure condition. As peak stress is approached, the rapid, fluid-driven growth of fracture networks downstream from the overpressured region provides a mechanism for fluid flow and fluid pressurization along segments of the fault outside the preexisting fluid reservoir. Propagation of high pore pressure fluids along fracture networks has been interpreted to drive earthquake nucleation (Sibson, 2007), aftershock sequences (Miller et al., 2004), and earthquake swarm activity (Horalek and Fischer, 2008). Invasion percolation processes are also employed in geothermal reservoir stimulation (Baisch et al., 2006). Dehydration and subsequent fluid pressure buildup is also invoked as a driver of seismicity in subducting slabs (Burlini et al., 2009).

The difference between fluid migration along tortuous, low aperture fracture arrays and short-circuit pathways along high-fracture-density shear failure zones has important implications for fluid flow in fracture-controlled hydrothermal mineralization environments. Tortuous, high surface area and thus high reactivity pathways along small fractures provide opportunities for efficient fluid-rock reaction (Cox, 2007), which could influence some ore deposition processes. In contrast, pervasive shear failure (permeability enhancement during a fault rupture event) provides potential for much more direct hydraulic connectivity between fluid reservoirs and sinks. This situation favors rapid transit of fluid to environments where they are out of equilibrium with their host rocks, and inhibits effective reaction along the pathway.

Repeated transitions from pervasive to localized flow, before and immediately after repeated rupture events, could make flow and reaction in hydrothermal systems particularly dynamic, especially if fracture permeability is sealed by mineral deposition between events. Permeability enhancement prior to peak stress (stress or fluid driven) may also be critical to understanding fluid storage and migration in hydrocarbon reservoirs or seal integrity in geosequestration and toxic waste containment projects. During time-dependent growth of fracture networks via invasion percolation processes, there is potential for reservoir leakage at stresses well below those required for macroscopic shear failure.

ACKNOWLEDGMENTS

Financial support from the Australian Research Council (grant DP0452448) and from the Netherlands Organisation for Scientific Research is acknowledged. Fracture length was calculated using the Dijkstra shortest path MATLAB routine of J. Kirk. Reviews by N. De Paola and two anonymous reviewers significantly improved the manuscript.

REFERENCES CITED

Baisch, S., Weidler, R., Vörös, R., Wyborn, D., and de Graf, L., 2006, Induced seismicity during the stimulation of a geothermal HFR reservoir in the Cooper Basin, Australia: Seismological Society of America Bulletin, v. 96, p. 2242–2256, doi: 10.1785/0120050255.

Berkowitz, B., 2002, Characterizing flow and transport in fractured geological media: A review: Advances in Water Resources, v. 25, p. 861–884, doi: 10.1016/S0309-1708(02)00042-8.

Burlini, L., Di Toro, G., and Meredith, P., 2009, Seismic tremor in subduction zones: Rock physics evidence: Geophysical Research Letters, v. 36, L08305, doi: 10.1029/2009GL037735.

Cox, S.F., 1999, Deformational controls on the dynamics of fluid flow in mesothermal gold systems, *in* McCaffrey, K., et al., eds., Fractures, fluid flow and mineralisation: Geological Society of London Special Publication 155, p. 123–139.

Cox, S.F., 2005, Coupling between deformation, fluid pressures, and fluid flow in ore-producing hydrothermal systems at depth in the crust, *in* Hedenquist, J.W., et al., eds., Economic Geology 100th anniversary volume: Denver, Colorado, Society of Economic Geologists, p. 39–75.

Cox, S.F., 2007, Structural and isotopic constraints on fluid flow regimes and fluid pathways during upper crustal deformation: An example from the Taemas area of the Lachlan Orogen, SE Australia: Journal of Geophysical Research, v. 112, B08208, doi: 10.1029/2006JB004734.

De Paola, N., Faulkner, D.R., and Collettini, C., 2009, Brittle versus ductile deformation as the main control on the transport properties of low porosity anhydrite rocks: Journal of Geophysical Research, v. 114, B06211, doi: 10.1029/2008JB005967.

Fischer, G.J., and Paterson, M.S., 1992, Measurements of permeability and storage capacity in rocks during deformation at high temperatures and pressures, *in* Evans, B., and Wong, T.-F., eds., Fault mechanics and transport properties of rocks: San Diego, California, Academic Press, p. 213–252.

Fredrich, J.T., Evans, B., and Wong, T.-F., 1990, Effect of grain size on brittle and semibrittle strength: implications for micromechanical modeling of failure in compression: Journal of Geophysical Research, v. 95, p. 10,907–10,920, doi: 10.1029/JB095iB07p10907.

Hickman, S., Sibson, R., and Bruhn, R., 1995, Introduction to special section: Mechanical involvement of fluids in faulting: Journal of Geophysical Research, v. 100, p. 12,831–12,840, doi: 10.1029/95JB01121.

Horalek, J., and Fischer, T., 2008, Role of crustal fluids in triggering the West Bohemia/Vogtland earthquake swarms: Just what we know: Studia Geophysica et Geodaetica, v. 52, p. 455–478, doi: 10.1007/s11200-008-0032-0.

Miller, S.A., Collettini, C., Chiaraluce, L., Cocco, M., Barchi, M., and Kaus, J.P., 2004, Aftershocks driven by a high-pressure CO_2 source at depth: Nature, v. 427, p. 724–727, doi: 10.1038/nature02251.

Peach, C.J., and Spiers, C.J., 1996, Influence of crystal plastic deformation on dilatancy and permeability development in synthetic salt rock: Tectonophysics, v. 256, p. 101–128, doi: 10.1016/0040-1951(95)00170-0.

Sahimi, M., 1994, Applications of percolation theory: London, Taylor and Francis, 258 p.

Sakellariou, A., Sawkins, T.J., Senden, T.J., and Limaye, A., 2004, X-ray tomography for mesoscale physics applications: Physica A, v. 339, p. 152–158, doi: 10.1016/j.physa.2004.03.055.

Sibson, R.H., 1996, Structural permeability of fluid-driven fault-fracture meshes: Journal of Structural Geology, v. 18, p. 1031–1042, doi: 10.1016/0191-8141(96)00032-6.

Sibson, R.H., 2000, Fluid involvement in normal faulting: Journal of Geodynamics, v. 29, p. 469–499, doi: 10.1016/S0264-3707(99)00042-3.

Sibson, R.H., 2007, An episode of fault-valve behaviour during compressional inversion? The 2004 M_J 6.8 Mid-Niigata Prefecture, Japan, earthquake sequence: Earth and Planetary Science Letters, v. 257, p. 188–199, doi: 10.1016/j.epsl.2007.02.031.

Stark, C.P., and Stark, J.A., 1991, Seismic fluids and percolation theory: Journal of Geophysical Research, v. 96, p. 8417–8426.

Tripp, G.I., and Vearncombe, J.R., 2004, Fault/fracture density and mineralization: A contouring method for targeting in gold exploration: Journal of Structural Geology, v. 26, p. 1087–1108, doi: 10.1016/j.jsg.2003.11.002.

Zhang, S., Cox, S.F., and Paterson, M.S., 1994, The influence of room-temperature deformation on porosity and permeability in calcite aggregates: Journal of Geophysical Research, v. 99, p. 15,761–15,775, doi: 10.1029/94JB00647.

Manuscript received 11 January 2010
Revised manuscript received 23 March 2010
Manuscript accepted 28 March 2010

Printed in USA